Science Advances
AAAS

Supplementary Materials for

Charting the nanotopography of inner hair cell synapses using MINFLUX nanoscopy

Rohan Kapoor *et al.*

Corresponding author: Tobias Moser, tmoser@gwdg.de

Sci. Adv. **11**, eady4344 (2025)
DOI: 10.1126/sciadv.ady4344

This PDF file includes:

Descriptions of alternative sample preparation approaches for MINFLUX
Supplementary Text for biophysical modeling
Figs. S1 to S10
Tables S1 to S7
References

Descriptions of alternative sample preparation approaches tested for MINFLUX imaging

HARD fixation

For HARD experiments (*33*), we used Ai32VC cre$^+$ mice (*17*) which express channelrhodopsin 2 (ChRh2) with a fluorescent EYFP tag under an IHC-specific VGLUT3 promoter. This approach allowed us to readily identify IHCs on coverslips. We adopted two approaches for heat-assisted immobilization of IHCs (Fig. S1):

1. Cochleae were dissected in ice-cold PBS. The round window of the cochlea was injected with 35% Pluronic gel (Pluronic F127 NF; BASF, Parsippany, NJ) using a pre-cooled syringe as described before (*119*) to support partitioning during cochlear sectioning. The cochlea was glued using cyanoacrylate on the stage of a slicing chamber filled with PBS at room temperature which causes Pluronic Gel to solidify. We then used a Leica VT1000s Vibratome to obtain 200 µm thick sections (slicing parallel to the cochlear modiolus, minimum speed and maximum frequency setting). Slices were immediately transferred to a poly-L-lysine coated coverslip maintained at 50°C on a hot plate. We tested different time durations ranging from 30 seconds to 5 minutes. The excess tissue was removed, and the coverslips were allowed to cure on the hot plate for another 5 minutes.
2. Cochleae were dissected in ice-cold PBS and the apical end of the organ of Corti was further dissected out and the tectorial membrane was carefully removed using a pair of fine forceps. The acute preparation of the organ of Corti was placed directly on a poly-L-lysine coated coverslip heated to 50°C on a hot plate for different time durations ranging from 30 seconds to 5 minutes. The excess tissue was removed, and the coverslips were allowed to cure on the hot plate for another 5 minutes. We tried placing the organ of Corti top-up with the basilar membrane towards the coverslip as well as tried positioning it in an inverted manner with the cuticular plate towards the coverslip. Both approaches yielded immobilized layers of cells on the coverslip.

After either approach, coverslips were immunostained with anti-chicken GFP (Abcam, ab13970) and anti-mouse CtBP2 (BD Biosciences, 612044) as described before in the methods section. With the first approach, results were largely inconsistent for us and in very few instances (2 out of 7 trials) we could obtain identifiable individual IHCs with synaptic ribbons on the coverslip. On the other hand, the second approach appeared more promising, with rows of identifiable IHCs with synaptic ribbons (Fig. S1B, C) in all experimental trials (N = 3). While the signal:noise ratio appeared optimal, MINFLUX did not work for these samples largely on account of larger distance of the synapses from the coverslip (>3 µm). It appeared this was due to IHCs sticking to the coverslip with either the basilar membrane in between, or IHCs were anchored from their apical end with the cuticular plate at the coverslip and the synapses away from it. An illustration depicting the two possible scenarios has been provided in Fig. S1D.

Cochlear Cryosections

Cryosections of cochleae from 2-week-old C57BL6/J mice were performed as described elsewhere (*84*). We collected the cryosections on poly-L-lysine coated coverslips (Fig. S1E) and tested sections of varying thicknesses ranging from 10 µm to 16 µm and found comparable results (representative immunostained section shown in Fig. S1F, G, H). While our initial attempts with MINFLUX imaging did not yield any results owing to high background fluorescence, treating the sections prior to blocking and immunostaining with 0.1% $NaBH_4$ solution (7 minutes) or 0.1M Tris (30 minutes) quenched tissue autofluorescence significantly. This allowed us to obtain some preliminary 2D (Fig. S1I) MINFLUX images of synaptic ribbons (RIBEYE), with suboptimal imaging quality. MINFLUX imaging of any other synaptic protein labelling did not work.

Supplementary text for biophysical modelling

Estimation of the local calcium concentration around synaptic vesicle sensors

We placed 6 Ca^{2+} sensors on the surface of the synaptic vesicle (SV). As the location of Ca^{2+} sensors is unknown, we first estimated the local [Ca^{2+}] around the SV (docked). To estimate local [Ca^{2+}] around sensors, we used "hits" as a proxy of the [Ca^{2+}] (*120*) where the number of hits represents the number of Ca^{2+} collisions on the SV surface estimated by MCell. At every time step of simulations, the number of hits and the location of the hit event were stored. As regions of the SV surface proximal to the $Ca_V1.3$ nanocluster exhibited higher hit rates compared to distal regions, we divided the SV surface into 648 discrete surfaces to reflect the spatial dependency of the local [Ca^{2+}]. We calculated the density of hits per unit area instead of summating over the whole surface as follows:

$$unit\ area\ = r^2 \cdot \cos\theta \cdot\ \delta\theta\ \cdot \delta\varphi$$

where θ is a polar angle ($0\ \leq \theta \leq \pi$) and φ is the azimuth angle ($-\pi \leq \varphi \leq \pi$). The polar angle was divided into 18 bins and the azimuth angle was divided into 36 bins. To convert the hit rates per unit area to the local calcium concentration, we ran simulations with one SV in a space filled with Ca^{2+} ions at [Ca^{2+}] of 20, 50, 100 μM. From these simulations, we could calculate the hit rate per unit area for each concentration. Then, we selected four-unit areas near the sensor 1 – which triggered the majority of release events - and plotted the mean of four unit areas (Fig. S9B). We summed the hit rate per unit area from t = 1.5 ms to t = 2 ms where the hit rate reaches the plateau for the single $Ca_V1.3$ nanocluster. Linear regression was used to estimate the local [Ca^{2+}] near sensor index 1, yielding an approximate value of 40 μM for the sensor index 1 in the single nanocluster case (hit rate per unit area ($\times 10^6$) = 5×10^4 [Ca^{2+}] + 15×10^4).

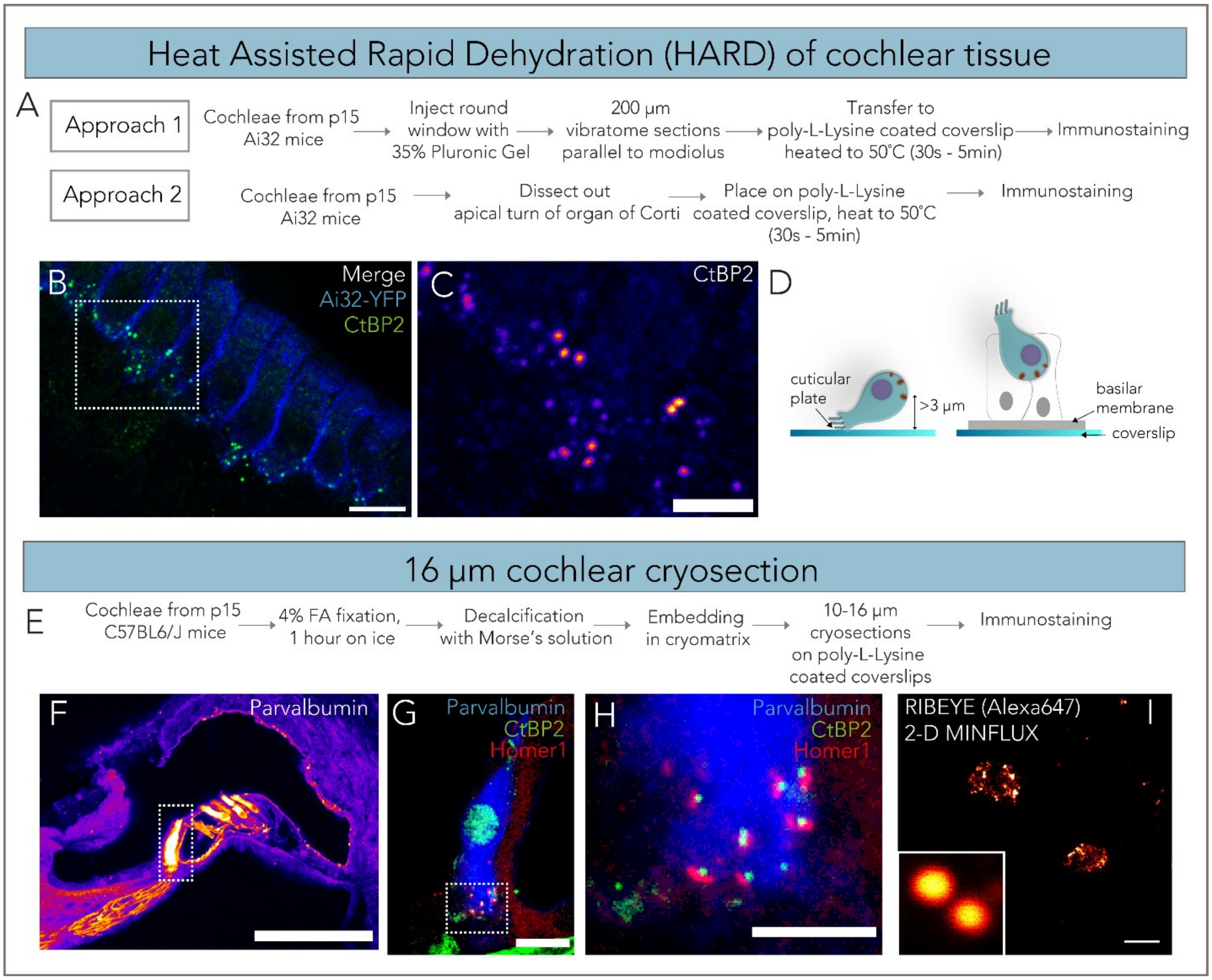

Fig. S1. Summary of alternative attempts at sample preparation for MINFLUX of IHC ribbon synapses

(A) Two alternative approaches towards Heat Assisted Rapid Dehydration (HARD) of cochlear tissue to fix IHCs on coverslip. Only approach 2 could be used for reproducible tissue immobilization on coverslips. **(B)** Confocal (single plane) image of HARD immobilized tissue from Ai32 mice showing IHC membrane (blue) and synaptic ribbons (CtBP2, green). Scale bar = 10 µm. **(C)** Confocal zoom-in showing synaptic ribbons in the region marked in (B). An intensity-coded look-up table has been used for depiction; scale bar = 5 µm. **(D)** IHCs appeared to be immobilized on the coverslips either via their apical end or via the basilar membrane, depending on the orientation of placement of the organ of Corti during HARD fixation. Either way, synapses were typically at a distance greater than 3 µm from the coverslip, making MINFLUX imaging difficult. **(E)** 10 – 16 µm cochlear cryosections for MINFLUX **(F)** Representative confocal overview of the organ of Corti from a 16 µm cochlear cryosection, scale bar = 100 µm. **(G, H)** Maximum-intensity projection of IHC marked in (F) shows ribbon synapses (CtBP2, green) and the postsynaptic density (Homer1, red). Scale bar = 10 and 5 µm for (G) and (H) respectively. **(I)** Exemplary 2D MINFLUX imaging of RIBEYE (Alexa 647) from a 16 µm cochlear cryosection. Inset shows corresponding confocal view of the two ribbons shown. Scale bar = 200 nm.

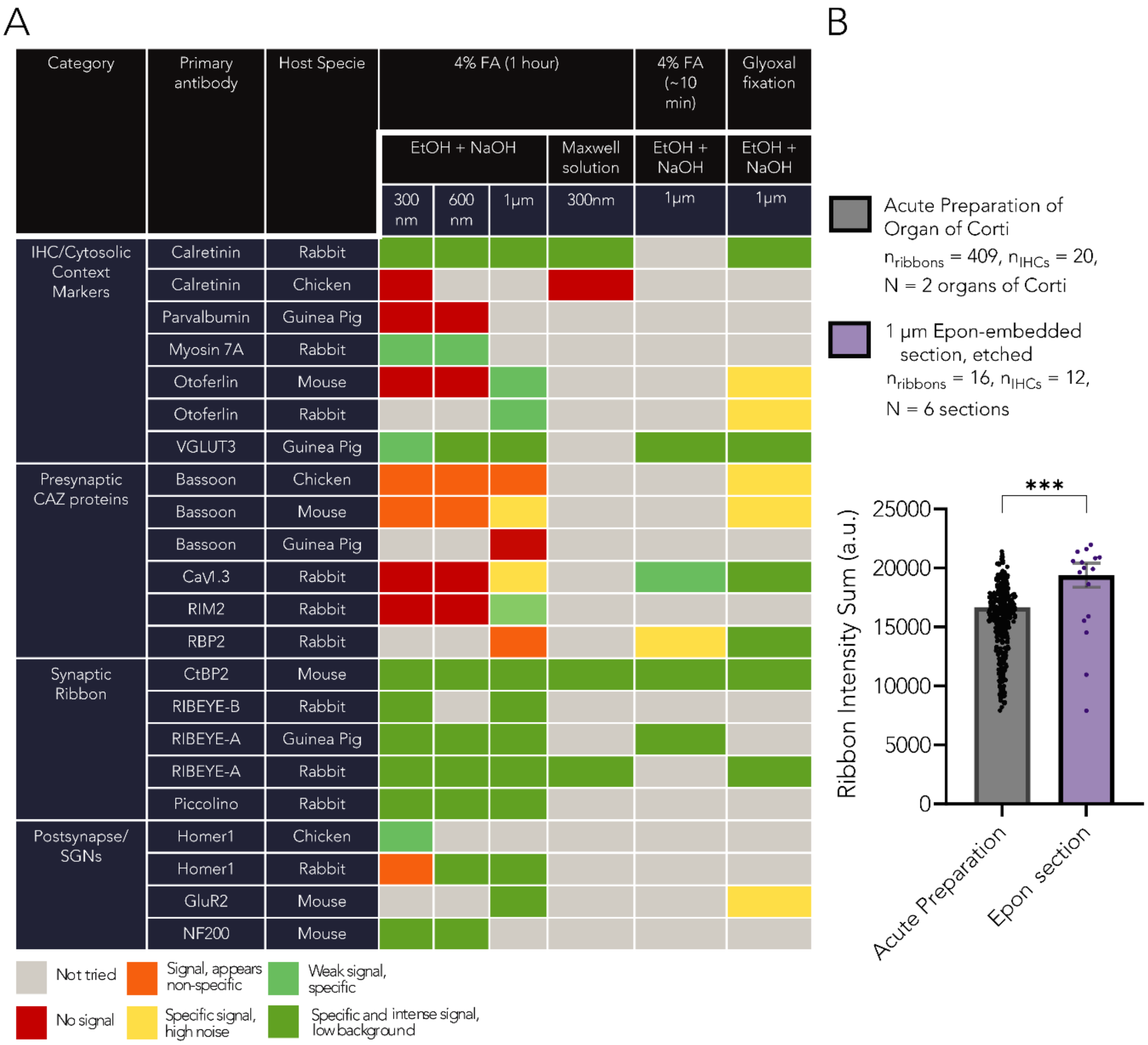

Category	Primary antibody	Host Specie	4% FA (1 hour)				4% FA (~10 min)	Glyoxal fixation
			EtOH + NaOH			Maxwell solution	EtOH + NaOH	EtOH + NaOH
			300 nm	600 nm	1µm	300nm	1µm	1µm
IHC/Cytosolic Context Markers	Calretinin	Rabbit	🟩	🟩	🟩	🟩	⬜	🟩
	Calretinin	Chicken	🟥	⬜	⬜	🟥	⬜	⬜
	Parvalbumin	Guinea Pig	🟥	🟥	⬜	⬜	⬜	⬜
	Myosin 7A	Rabbit	🟢	🟢	⬜	⬜	⬜	⬜
	Otoferlin	Mouse	🟥	🟥	🟢	⬜	⬜	🟨
	Otoferlin	Rabbit	⬜	⬜	🟢	⬜	⬜	🟨
	VGLUT3	Guinea Pig	🟢	🟩	🟩	⬜	🟩	🟩
Presynaptic CAZ proteins	Bassoon	Chicken	🟧	🟧	🟧	⬜	⬜	🟨
	Bassoon	Mouse	🟧	🟧	🟨	⬜	⬜	🟨
	Bassoon	Guinea Pig	⬜	⬜	🟥	⬜	⬜	⬜
	Ca$_V$1.3	Rabbit	🟥	🟥	🟨	⬜	🟢	🟩
	RIM2	Rabbit	🟥	🟥	🟢	⬜	⬜	⬜
	RBP2	Rabbit	⬜	⬜	🟧	⬜	🟨	🟩
Synaptic Ribbon	CtBP2	Mouse	🟩	🟩	🟩	🟩	🟩	🟩
	RIBEYE-B	Rabbit	🟩	⬜	🟩	⬜	⬜	⬜
	RIBEYE-A	Guinea Pig	🟩	🟩	🟩	⬜	🟩	⬜
	RIBEYE-A	Rabbit	🟩	🟩	🟩	🟩	⬜	🟩
	Piccolino	Rabbit	🟩	🟩	🟩	⬜	⬜	⬜
Postsynapse/ SGNs	Homer1	Chicken	🟢	⬜	⬜	⬜	⬜	⬜
	Homer1	Rabbit	🟧	🟩	🟩	⬜	⬜	⬜
	GluR2	Mouse	⬜	⬜	🟩	⬜	⬜	🟨
	NF200	Mouse	🟩	🟩	⬜	⬜	⬜	⬜

⬜ Not tried
🟥 No signal
🟧 Signal, appears non-specific
🟨 Specific signal, high noise
🟢 Weak signal, specific
🟩 Specific and intense signal, low background

Fig. S2. Optimization of immunostainings of semithin sections from Epon embedded cochleae after etching

(A) Summary of primary antibody stainings attempted on sections of varying thickness (300 nm, 600 nm and 1 µm) and the subjective quality of stainings have been denoted with a colour code. Several immunostainings that did not work for thinner sections showed drastic improvement on switching to 1 µm sections, possibly because of more intact synaptic structures. In addition to etching samples with NaOH and ethanol, we initially also performed etching of 300 nm thin sections with Maxwell solution (*122*) and found very comparable results. Immunolabeling for RBP2 and Ca$_V$1.3 showed poor results when cochleae were fixed with 4% formalin for 1 hour. The quality of stainings for these improved upon a shorter fixation duration for ~10 minutes and was the most optimal with glyoxal fixation. **(B)** Intensity of immunostained synaptic ribbons was compared between acute preparations of the organ of Corti and Epon-embedded and etched 1 µm sections. The samples were both from postnatal day 15 C57BL/6J mice, fixed for 1 hour with 4% formalin, decalcified with Morse's solution, were stained with the same antibody concentrations and imaged with the same laser settings in parallel. Epon embedding and etching the samples with NaOH and ethanol does not seem to reduce immunofluorescence signal intensity, suggesting that epitopes are preserved well through the process.

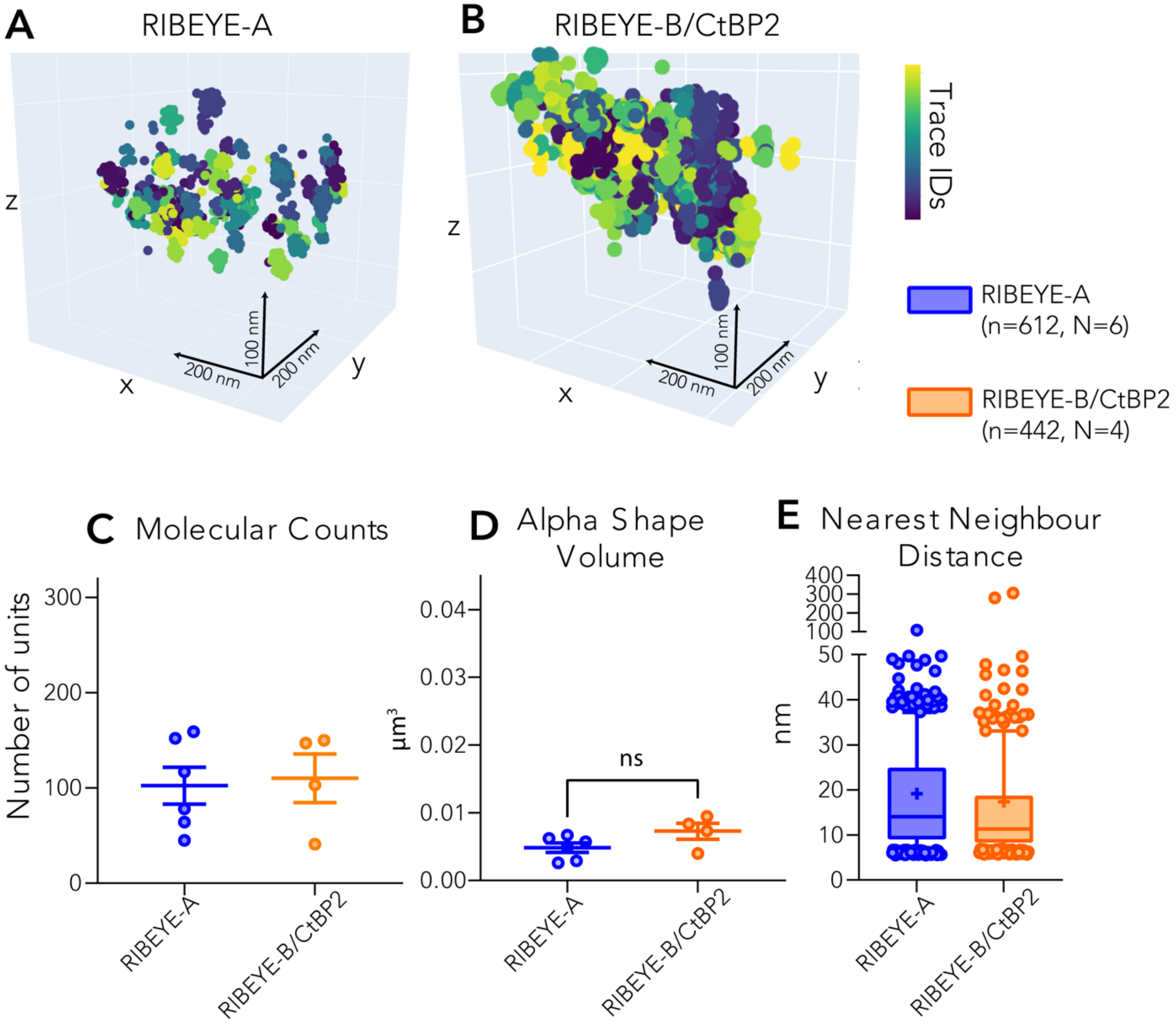

Fig. S3. 3D MINFLUX imaging of synaptic ribbons using two different antibodies labelling N- and C-terminal domains of RIBEYE

Raw 3D MINFLUX data of synaptic ribbons labelled with **(A)** anti-RIBEYE A domain or **(B)** anti-CtBP2 (RIBEYE B domain) primary antibodies respectively. Images acquired from different synapses; colour scale is indicative of Trace IDs. The 3D spatial arrangement of RIBEYE within the synaptic ribbon appears comparable irrespective of which RIBEYE domain was immunolabelled. Molecular counts **(C)**, alpha shape volume fits **(D)** and nearest neighbour distance estimates **(E)** are also comparable. In (C) and (D), plots depict mean ± SEM and data points represent individual synapses. In (E), box-whisker plots have crosses representing mean values, central band indicates the median, whiskers represent 90/10 percentiles and boxes represent 75/25 percentiles; individual data points represent molecular counts. Data is not significantly different in (D), Wilcoxon's Rank Test ($P > 0.05$); n = number of molecular counts, N = number of synapses.

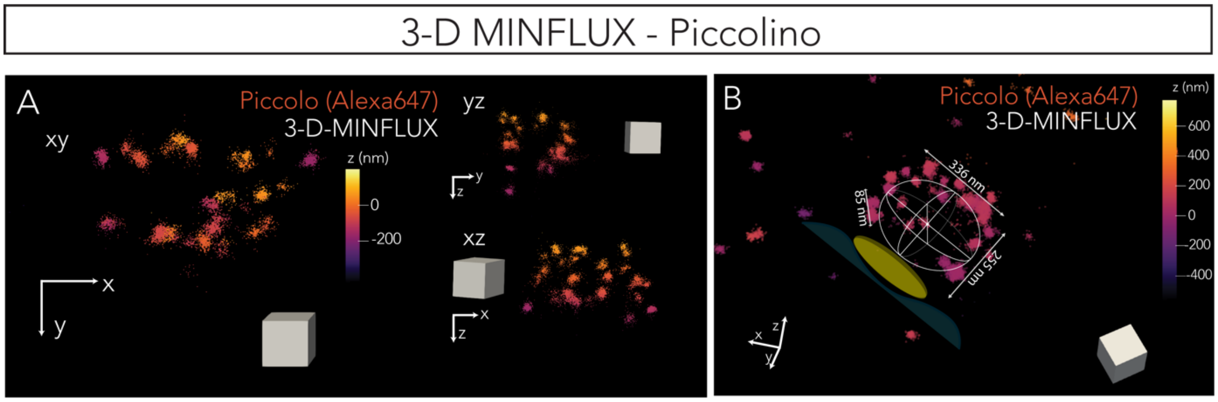

Fig. S4. 3D MINFLUX images of Piccolino show an arch-shaped structure that envelops the synaptic ribbon

(A) Representative 3D MINFLUX image of Piccolino (labelled with an antibody recognizing amino acid 2012–2351 of rat Piccolo), shows a characteristic arch shaped structure along the z-projection. Projections along the x- and y- axes have also been depicted. **(B)** Another exemplary 3D MINFLUX image of Piccolino from a different IHC. An illustrated ellipsoid showing the likely position of the synaptic ribbon inside the Piccolino arch has been overlaid. The image has been tilted as shown by the orientation axis in the left corner to better reveal the structure. Colour codes represent the distances along the z-axis; the cube shown for scale has an edge of length 100 nm.

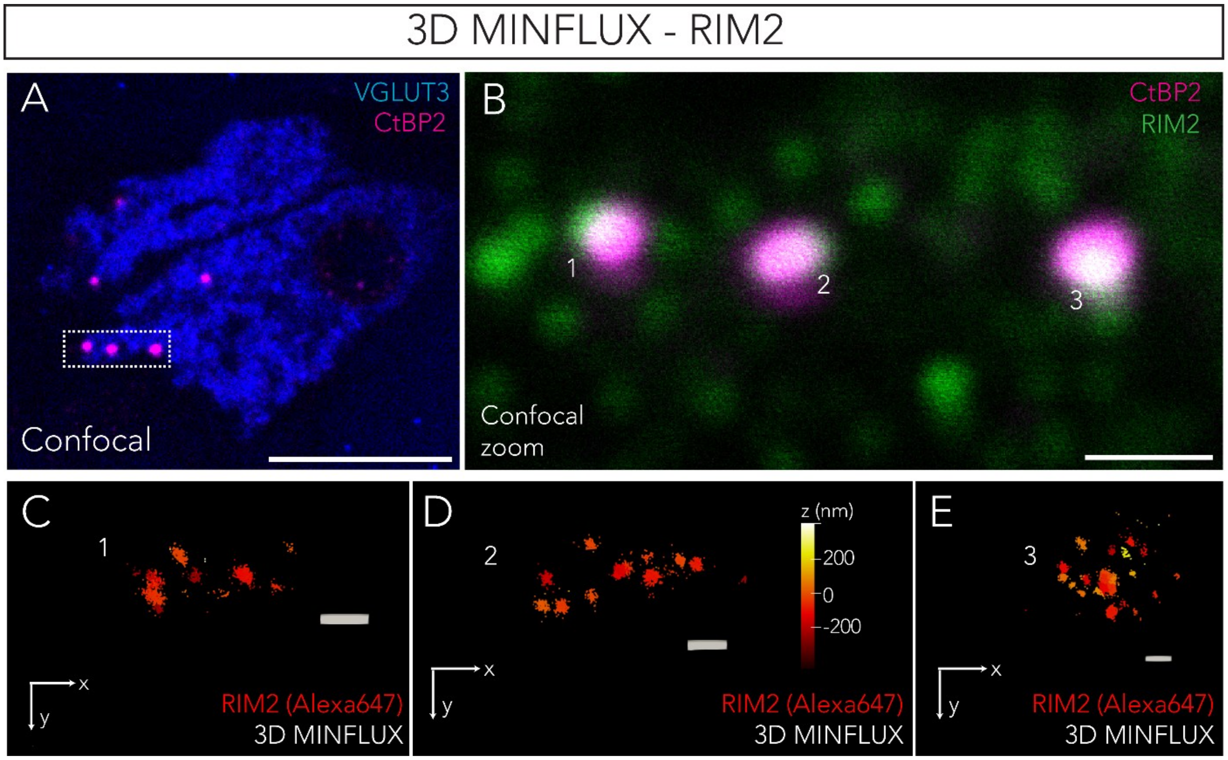

Fig. S5. 3D MINFLUX images of AZ protein RIM2

(A) Representative confocal overview (single plane) of IHC used for imaging (VGLUT3, blue) and the location of the ribbon synapses in the cell (CtBP2, magenta). Scale bar = 10 µm. **(B)** Zoom-in of the ribbon synapses. Here the corresponding RIM2 puncta have been imaged (green). Scale bar = 1 µm. **(C, D, E)** Z-projections of 3D MINFLUX images of RIM2 from the synapses marked in (B) shows the topographic distribution of the protein at the AZ. Colour code represents distances along the z-axis and scale bar has a length of 100 nm.

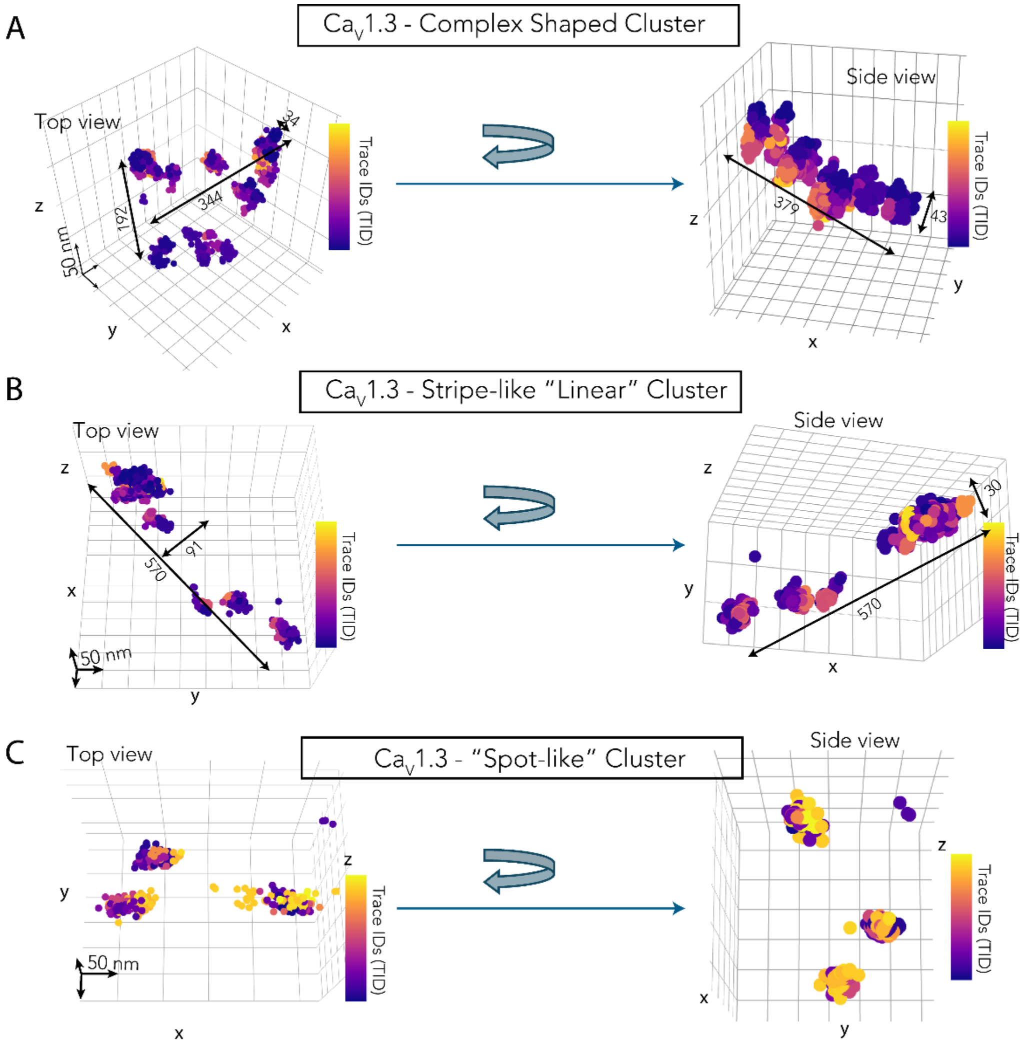

Fig. S6. Heterogeneous morphology of Ca$_V$1.3 channel clusters in 3D MINFLUX images. Further exemplary synapses (raw 3D MINFLUX data) illustrating the heterogeneity in morphology of Ca$_V$1.3 channel clusters observed in IHCs. **(A)** Distribution of Ca$_V$1.3 localisations shows a complex spatial arrangement when viewed from the top, however rotating the image displays a linear arrangement of the localisations along the side, likely presenting a view along the plasma membrane as also shown in Fig. 2H. Such "complex" channel clusters account for 44.5% of synapses in our data. **(B)** A linear, stripe-like Ca$_V$1.3 cluster; the stripe-like appearance is evident irrespective of the orientation in which the synapse is viewed. Such synapses also make up 44.5% of the total synapses we imaged. **(C)** Small "spot-like" Ca$_V$1.3 cluster with no define morphology; these constitute the remaining 11% of synapses in our data. Representative measures of dimensions have been depicted with arrows; scale of grid lines is 50 nm along all dimensions and colour code represents Trace IDs of individual localisations.

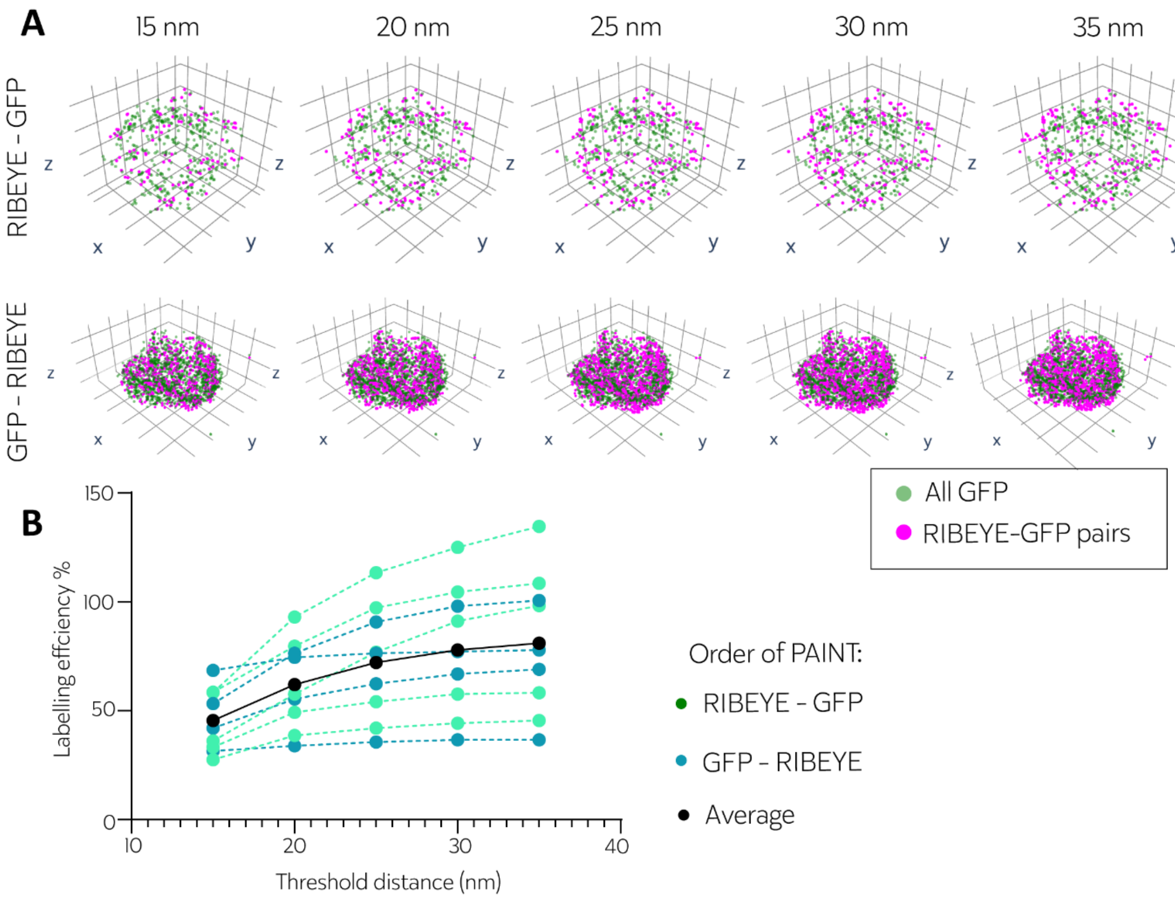

Fig. S7. Estimation of relative labelling efficiency of anti-RIBEYE primary antibody compared to anti-GFP nanobody in HEK293 cells expressing RIBEYE-GFP
To assess the relative labelling efficiency, we transfected HEK293 cells with RIBEYE-GFP and imaged the cytosolic RIBEYE-GFP clusters with DNA-PAINT MINFLUX imaging. **(A)** Post-correction localisations were aggregated based on their TraceIDs to obtains centroids which have been depicted from individual RIBEYE-GFP cytosolic clusters. Green points represent GFP centroids, while magenta points represent RIBEYE centroids paired with GFP centroids for pairing thresholds of 15 – 35 nm. We performed PAINT in variable sequences: RIBEYE first and GFP later and vice versa to minimize the effects of photobleaching; data from exemplary RIBEYE-GFP clusters has been shown for both scenarios. **(B)** Relative labelling efficiency calculated as the ratio of number of RIBEYE-GFP centroid pairs to the total number of GFP centroids for different pairing thresholds. Different shades of green represent the sequence in which PAINT was performed as described in the legend. Each dotted line represents an individual RIBEYE-GFP clusters (n = 9 clusters from N = 4 cells).

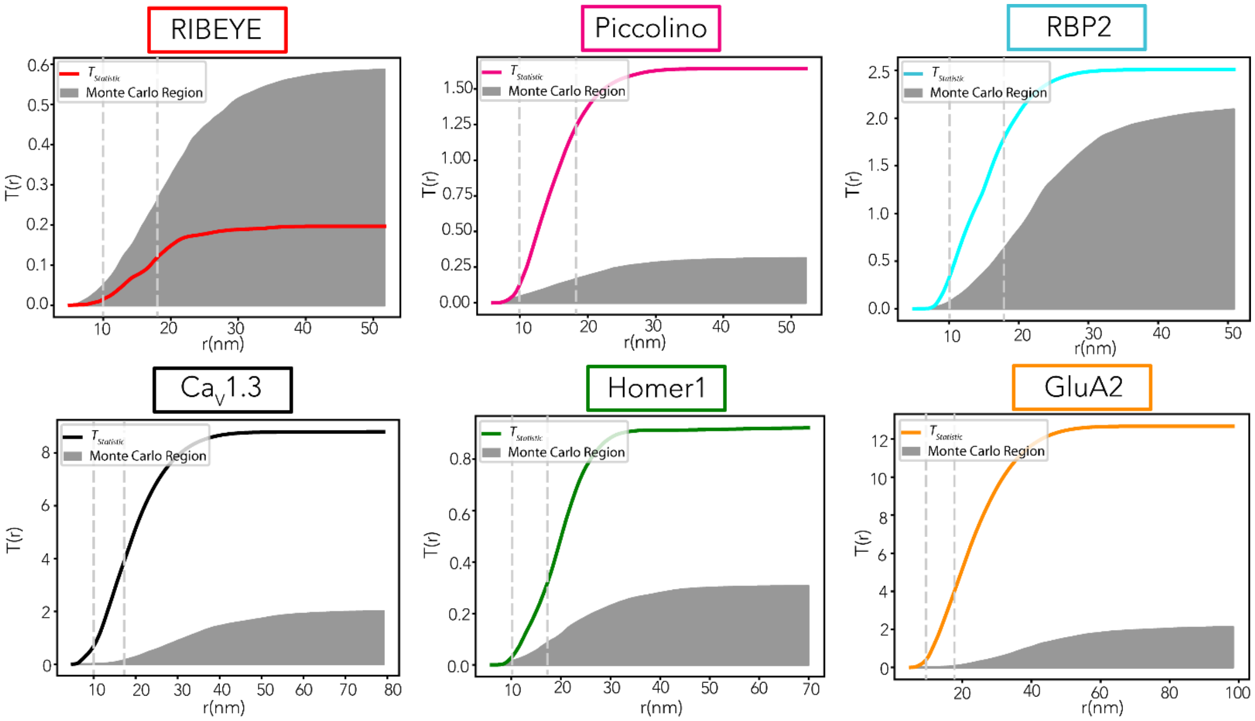

Fig. S8. Envelop representation of DCLF Test

Exemplary envelope representations for the Diggle-Cressie Loosmore-Ford (DCLF) test of spatial randomness (SR) confined to protein molecule's convex hull, applied to the data of Fig. 6, and considering the full range of distance values from experiment localization precision to tens of nanometres. Vertical lines represent the evaluation interval. DCLF test statistic T (solid-coloured lines) and Monte Carlo acceptance/non-rejection region (shaded) have been plotted as a function of the length r of the distance interval. Graphs based on 1000 simulations of SR.

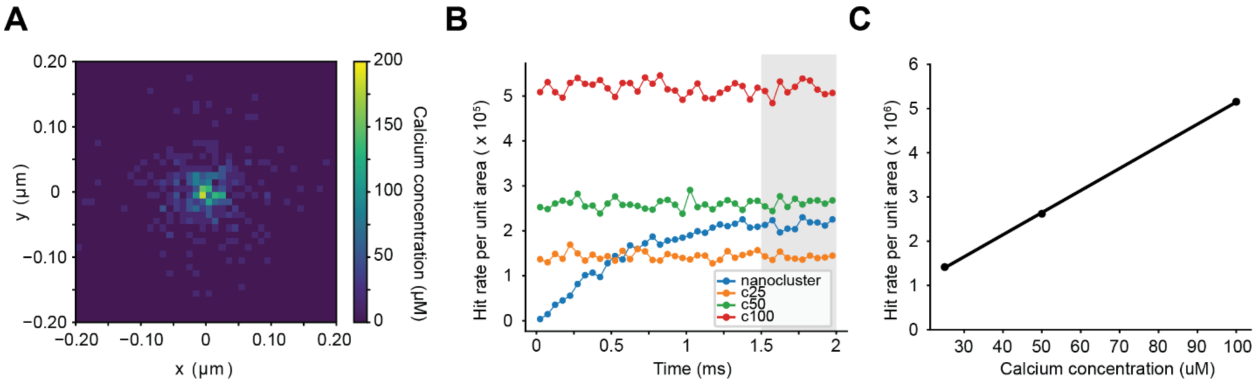

Fig. S9. Estimation of the local calcium concentration at SV for a single Ca$_{V}$1.3 nanocluster. **(A)** Calcium concentration map of a single Ca$_{V}$1.3 nanocluster. Each pixel represents a voxel with a size of 10 nm × 10 nm × 10 nm. The range of z is from 0 to 10 nm. Color bar indicates the range of calcium concentration (unit: µM). **(B)** The plot of hit rate per unit area in time for four selected SV surface regions located near sensor index 1. Each trace corresponds to the single Ca$_{V}$1.3 nanocluster case (blue) and the conditions with fixed calcium concentrations of 25, 50, and 100 µM (orange, green, red, respectively). The shaded grey region (1.5 – 2.0 ms) indicates the plateau phase in the single nanocluster case (blue). **(C)** The fitted curve showing the relationship between the calcium concentration and the summation of the hit rate per unit area within the time window of 1.5 – 2.0 ms.

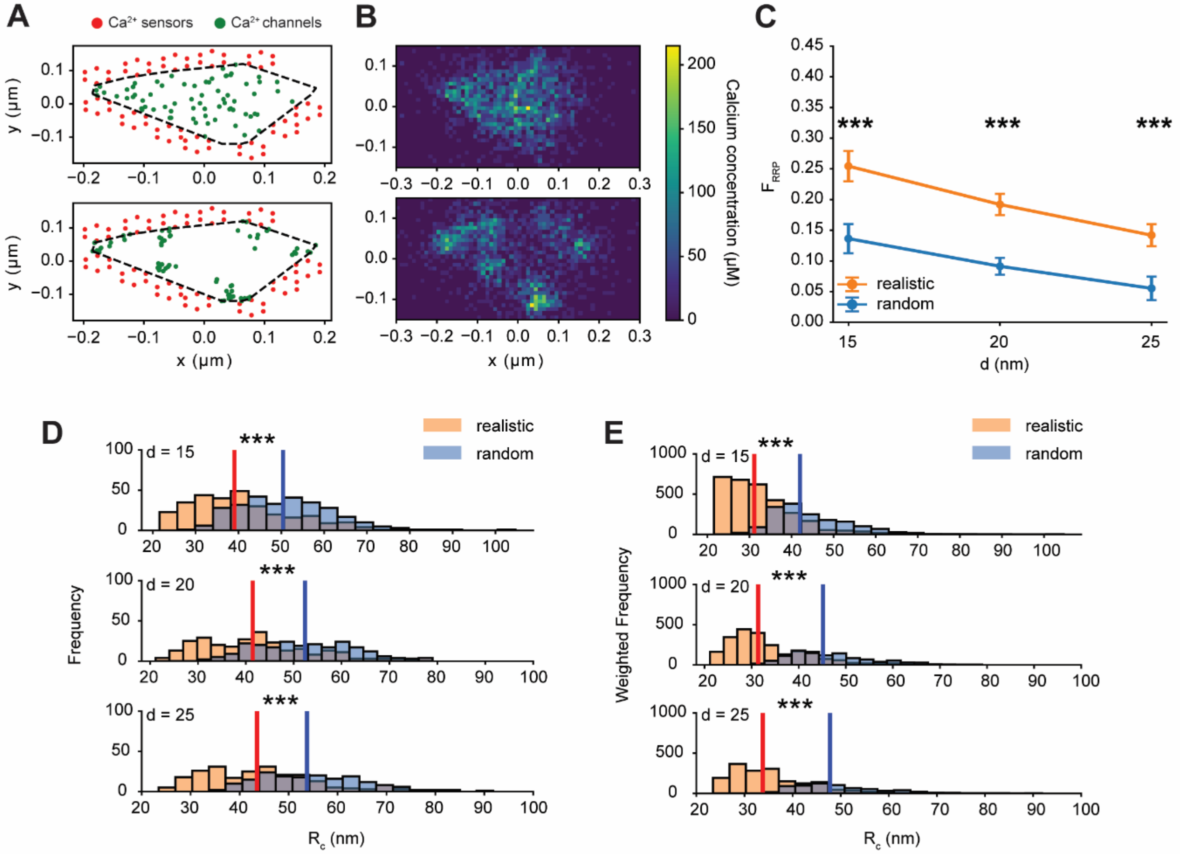

Fig. S10. Model of one imaged exemplarily AZ with both Ca^{2+} channels nanoclusters and non-clustered Ca^{2+} channels. **(A)** Top view of one of 10 different spatial distributions of 70 Ca^{2+} channels in random (artificial, top) or CaV1.3 nanocluster (experimentally observed, bottom) configurations, simulating a realistic scenario derived from our 3D MINFLUX data of CaV1.3. **(B)** Ca^{2+} concentration $[Ca^{2+}]$ estimated with a voxel size of 10 nm x 10 nm x 10 nm. Range of z-axis is from 0 nm to 10 nm. Colour bar indicates the range of $[Ca^{2+}]$ in µM. **(C)** Release probability as a function of coupling distance d for realistic scenarios (orange) and random (blue) scenarios; error bars indicate standard deviations, and statistical significance is marked (t-test, *** $P < 0.001$). **(D)** Histograms of R_c at different d values (d = 15, 20, 25 nm), comparing realistic (orange) and random (blue) scenarios; statistical significance is indicated (Mood's median test, ** $P < 0.01$, *** $P < 0.001$). Red and blue lines indicate median for nanocluster and random scenario respectively. **(E)** Weighted frequency histograms of R_c (incorporating number of release events per bin) for different d values, (t- test, *** $P < 0.001$).

Table S1. Comparison of synaptic dimensions measured by different modalities

		3D-MINFLUX	**Super-resolution STED imaging**	**Electron Microscopy**
Dimensions	**Synaptic ribbon**	400 X 150 X 200 nm *(l X w x h)*	~150 X 180 nm *(w X h)* (*54*)	400 X 120 X 190 nm *(l X w X h)* (*1*, *21*, *65*)
	Active Zone	422 X 102 X 47 nm *(linear Ca$_V$1.3 clusters, l X w x h)* 382 X 94 X 60 nm *(l X w X h, RBP2)*	~450 X 70 nm *(l X h, 3D and 2D STED resp., Ca$_V$1.3 and Bassoon)* (*18*)	~120 nm *(presynaptic density length)* (*6*, *14*)
	Postsynapse	800 X 300 X 100 nm *(Homer1, l X w X h)* 790 nm *(GluA2, peak-to-peak distance)*	~900 nm *(GluA2, peak-to-peak distance)* (*65*, *66*)	~ 900 nm *(PSD length)* (*65*)

Table S2. Summary of different morphologies of Ca$_V$1.3 clusters and quantified parameters

Ca$_V$1.3 clusters were classified into “lines”, “complexes” or “spot-like” as also depicted in Fig. S6. For tapered synapses (see Fig. S6A), where one end appeared broader than the other end, we measured the width along the two ends and reported the average. For two “complex” and all “spot-like” synapses, measuring the three dimensions was not possible due to the irregular shape of the synapse (denoted as not applicable, “NA” in the table below). For four synapses (all lines), DCLF test indicated non-clustered spatial arrangement of molecular counts. For these synapses, nanocluster parameters were not quantified (denoted with a ‘-’).

N	**Morphology**	**Length (nm)**	**Width (nm)**	**Height (nm)**	**Mol. Counts**	**Alpha Shape Volume (µm^3)**	**No. of nano clusters**	**Average no. of channels/ nanocluster**	**Average Inter-cluster NND (nm)**	**Average Intra-cluster NND (nm)**
1	line	673.5	156.6	61.3	24	4.0E-04	-	-	-	-
2	line	359.4	152.7	69.7	42	1.3E-03	6	7	100.3	12.7
3	line	224.1	84.3	49.9	41	2.7E-04	-	-	-	-
4	line	414.2	97.3	55.3	28	9.0E-04	-	-	-	-
5	line	565.5	91.4	29.9	57	6.3E-04	7	7	64.0	8.6
6	line	455.6	84.1	39.7	51	2.0E-03	5	10	103.1	9.0
7	line	441.5	114.6	53.8	27	8.5E-04	2	10	131.8	13.8
8	line	241.1	38.3	20.2	12	6.0E-05	-	-	-	-
Average (lines only)		**421.9**	**102.4**	**47.5**	**35**	**8.0E-04**	**5**	**8**	**99.8**	**11.0**
9	complex	479.6	190.6	52.3	43	2.1E-03	4	10	211.9	10.4
10	complex	267.5	174.6	57.6	66	3.1E-03	5	12	103.9	9.3
11	complex	388.6	146.9	43.1	70	1.6E-03	7	8	84.3	10.1
12	complex	484.9	156.6	48.2	40	2.5E-03	5	6	84.8	10.6
13	complex	NA	NA	NA	17	1.4E-03	3	4	195.7	14.0
14	complex	466.0	266.0	40.1	45	2.1E-03	8	5	114.5	11.9
15	complex	253.9	128.2	19.4	9	9.9E-05	2	4	215.6	8.4
16	complex	NA	NA	NA	23	1.5E-03	5	4	117.8	12.2
Average (complexes only)		**390.1**	**177.1**	**43.4**	**39**	**1.8E-03**	**5**	**7**	**141.1**	**10.9**
17	spot-like	NA	NA	NA	17	6.5E-03	3	5	232.9	28.7
18	spot-like	NA	NA	NA	23	5.1E-04	3	7	140.3	9.3
Average (spot-like only)		**NA**	**NA**	**NA**	**20**	**3.5E-03**	**3**	**6**	**186.6**	**19.0**
Average (all)		**408.2**	**134.4**	**45.7**	**35**	**1.5E-03**	**5**	**7**	**135.8**	**12.1**

Table S3. Parameters for biophysical modelling

Parameter	**Value**				**Reference**
	Concentration	Diffusion Constants $[\mu m^2 ms^{-1}]$	K_D $[\mu M]$	k_{on} $[\mu M^{-1} ms^{-1}]$	
Fixed Buffers	610 µM		4.859	1.375	(*122*)
EGTA	800 µM	0.14	0.071	0.0105	(*123*, *124*)
BAPTA	400 µM	0.14	0.17	0.45	(*124*, *125*)
ATP	68 µM (Calculated in 3mM Mg^{2+} 2mM ATP)	0.14	2200	0.013	(*126*)
Resting Ca^{2+} concentration	50 nM	0.223			(*96*, *127*)

Table S4. List of primary antibodies

Antibody	Host specie	Epitope	Dilution	Company	Identifier
Anti-Calretinin	Rabbit Polyclonal	-	1:200	Swant	CR7697
Anti-Calretinin	Chicken Polyclonal	Full length recombinant mouse Calretinin (UniProt ID: Q08331)	1:200	Synaptic Systems	214106
Anti-Parvalbumin	Guinea Pig Polyclonal	-	1:200	Synaptic Systems	195004
Anti-MyoVIIA	Rabbit Polyclonal	AA 880 – 1077 of tail region of human myosin-VIIa	1:200	Proteus	25-6790-C050
Anti-Otoferlin	Mouse Monoclonal	AA 1 – 400 of recombinant human Otoferlin	1:200	Abcam	ab53233
Anti-Otoferlin	Rabbit Polyclonal	AA 181 – 196 of mouse Otoferlin (UniProt ID: Q9ESF1-1)	1:200	Synaptic Systems	178003
Anti-VGLUT3	Guinea Pig Polyclonal	AA 543 – 601 of mouse VGLUT3 (UniProt ID Q8BFU8)	1:200	Synaptic Systems	135204
Anti-$Ca_V1.3$	Rabbit Polyclonal	AA 859 – 875 of rat $Ca_V1.3$ (Accession P27732), intracellular loop between domains II and III	1:100	Alomone	ACC-005
Anti-RIM2	Rabbit Polyclonal	AA 461 – 987 of rat RIM2 (PDZ domain)	1:200	Synaptic Systems	140103
Anti-RBP2	Rabbit Polyclonal	AA 596 – 868 of mouse RBP2 (UniProt ID Q80U40)	1:200	Synaptic Systems	316103
Anti-CtBP2	Mouse Monoclonal IgG1	Mouse CtBP2 AA 361 – 445	1:200	BD Biosciences	612044
Anti-RIBEYE-B	Rabbit Polyclonal	AA 974 – 988 of rat RIBEYE (UniProt ID Q9EQH5-2)	1:200	Synaptic Systems	192003
Anti-RIBEYE-A	Rabbit Polyclonal	AA 95 – 207 of rat RIBEYE (UniProt ID Q9EQH5-2)	1:200	Synaptic Systems	192103
Anti-RIBEYE-A	Guinea Pig Polyclonal	AA 95 – 207 of rat RIBEYE (UniProt ID Q9EQH5-2)	1:200	Synaptic Systems	192104
Anti-Piccolo	Rabbit Polyclonal	AA 2011 – 2350 of rat Piccolo (UniProt ID Q9JKS6)	1:200	Synaptic Systems	142113
Anti-Bassoon	Chicken Polyclonal	Recombinant protein corresponding to central region rat Bassoon (UniProt Id: O88778)	1:200	Synaptic Systems	141016
Anti-Bassoon	Guinea Pig Polyclonal	Recombinant protein corresponding to central region rat Bassoon (UniProt Id: O88778)	1:200	Synaptic Systems	141004
Anti-Bassoon	Mouse Monoclonal IgG2a	AA 756 – 1001 of mouse Bassoon (clone SAP7F407)	1:200	Abcam	Ab82958
Anti-Homer1	Rabbit Polyclonal	N-terminal of human Homer1 (UniProt ID Q86YM7)	1:200	Synaptic Systems	160002
Anti-Homer1	Chicken Polyclonal	Recombinant protein corresponding to N-terminal	1:200	Synaptic Systems	160006

		of human Homer1 (UniProt ID: Q86YM7)			
Anti-GluA2	Mouse Monoclonal IgG2a	GluA2 extracellular (putative N-terminal portion, AA 175 – 430), UniProt ID P19491	1:200	Merck Millipore	MAB397
Anti-NF200	Mouse Monoclonal IgG1	Neurofilament Heavy Chain (200 kDa) clone NE14	1:200	Sigma Aldrich	N5389

Table S5. List of secondary antibodies

Antibody	Host specie	Dilution	Company	Identifier
Alexa 488 conjugated anti-rabbit	Goat IgG (H+L)	1:200	Invitrogen	A11008
Alexa 488 conjugated anti-chicken	Goat IgG (H+L)	1:200	Invitrogen	A11039
Alexa 488 conjugated anti-guinea pig	Goat IgG (H+L)	1:200	Invitrogen	A11073
Alexa 488 conjugated anti-mouse	Goat IgG (H+L)	1:200	Invitrogen	A11001
Alexa 546 conjugated anti-mouse	Goat IgG (H+L)	1:200	Invitrogen	A11003
Alexa 647 conjugated anti-rabbit	Goat IgG (H+L)	1:200	Invitrogen	A21244
Alexa 647 conjugated anti-mouse	Goat IgG (H+L)	1:200	Invitrogen	A21236
Alexa 647 conjugated anti-mouse	Goat IgG2a	1:200	Invitrogen	A21241
Alexa 647 conjugated anti-chicken	Goat IgG (H+L)	1:200	Invitrogen	A21449
CF660C conjugated anti-mouse	Goat IgG (H+L)	1:200	Biotium	20052-1
CF660C conjugated anti-guinea pig	Goat IgG (H+L)	1:200	Biotium	20497-1

Table S6. 2D MINFLUX sequence parameters

Iteration	L (nm)	Photon threshold	CFR threshold	Dwell time (ms)	Pattern Repeats	Background offset (kHz)	Power factor
0	288	160	-1	1	1	15	1
1	288	150	-1	1	5	10	1
2	151	100	0.8	1	5	10	2
3	76	100	0.8	1	5	10	4
4	40	150	*	1	5	10	6

*= checked, no threshold applied; CFR = Centre Frequency Ratio

Table S7. 3D MINFLUX sequence parameters

Iteration	L (nm)	Photon threshold	CFR threshold	Dwell time (ms)	Pattern Repeats	Background offset (kHz)	Power factor
0	288	160	-1	1	1	15	1
1	288	400	-1	1	1	15	1
2	288	100	-1	1	5	10	1
3	288	50	-1	1	5	10	1
4	151	67	0.9	1	5	10	2
5	151	33	-1	1	5	10	2
6	76	67	0.8	1	5	10	4
7	76	33	-1	1	5	10	4
8	40	100	-1	1	5	10	6
9	40	50	-1	1	5	10	6

CFR = Centre Frequency Ratio

REFERENCES AND NOTES

1. T. Moser, C. P. Grabner, F. Schmitz, Sensory processing at ribbon synapses in the retina and the cochlea. *Physiol. Rev.* **100**, 103–144 (2019).

2. R. G. Zhai, H. J. Bellen, The architecture of the active zone in the presynaptic nerve terminal. *Physiology (Bethesda)* **19**, 262–270 (2004).

3. C. Wichmann, T. Moser, Relating structure and function of inner hair cell ribbon synapses. *Cell Tissue Res.* **361**, 95–114 (2015).

4. F. Schmitz, A. Königstorfer, T. C. Südhof, RIBEYE, a component of synaptic ribbons: A protein's journey through evolution provides insight into synaptic ribbon function. *Neuron* **28**, 857–872 (2000).

5. S. Maxeiner, F. Luo, A. Tan, F. Schmitz, T. C. Südhof, How to make a synaptic ribbon: RIBEYE deletion abolishes ribbons in retinal synapses and disrupts neurotransmitter release. *EMBO J.* **35**, 1098–1114 (2016).

6. P. Jean, D. L. de la Morena, S. Michanski, L. M. J. Tobón, R. Chakrabarti, M. M. Picher, J. Neef, S. Jung, M. Gültas, S. Maxeiner, A. Neef, C. Wichmann, N. Strenzke, C. Grabner, T. Moser, The synaptic ribbon is critical for sound encoding at high rates and with temporal precision. *eLife* **7**, e29275 (2018).

7. L. Becker, M. E. Schnee, M. Niwa, W. Sun, S. Maxeiner, S. Talaei, B. Kachar, M. A. Rutherford, A. J. Ricci, The presynaptic ribbon maintains vesicle populations at the hair cell afferent fiber synapse. *eLife* **7**, e30241 (2018).

8. V. G. Magupalli, K. Schwarz, K. Alpadi, S. Natarajan, G. M. Seigel, F. Schmitz, Multiple RIBEYE-RIBEYE interactions create a dynamic scaffold for the formation of synaptic ribbons. *J. Neurosci.* **28**, 7954–7967 (2008).

9. H. Regus-Leidig, C. Ott, M. Löhner, J. Atorf, M. Fuchs, T. Sedmak, J. Kremers, A. Fejtová, E. D. Gundelfinger, J. H. Brandstätter, Identification and immunocytochemical characterization

of Piccolino, a novel Piccolo splice variant selectively expressed at sensory ribbon synapses of the eye and ear. *PLOS ONE* **8**, e70373 (2013).

10. T. M. Müller, K. Gierke, A. Joachimsthaler, H. Sticht, Z. Izsvák, F. K. Hamra, A. Fejtová, F. Ackermann, C. C. Garner, J. Kremers, J. H. Brandstätter, H. Regus-Leidig, A multiple Piccolino-RIBEYE interaction supports plate-shaped synaptic ribbons in retinal neurons. *J. Neurosci.* **39**, 2606–2619 (2019).

11. S. Michanski, R. Kapoor, A. M. Steyer, W. Möbius, I. Früholz, F. Ackermann, M. Gültas, C. C. Garner, F. K. Hamra, J. Neef, N. Strenzke, T. Moser, C. Wichmann, Piccolino is required for ribbon architecture at cochlear inner hair cell synapses and for hearing. *EMBO Rep.* **24**, e56702 (2023).

12. D. Lenzi, J. W. Runyeon, J. Crum, M. H. Ellisman, W. M. Roberts, Synaptic vesicle populations in saccular hair cells reconstructed by electron tomography. *J. Neurosci.* **19**, 119–132 (1999).

13. D. Lenzi, J. Crum, M. H. Ellisman, W. M. Roberts, Depolarization redistributes synaptic membrane and creates a gradient of vesicles on the synaptic body at a ribbon synapse. *Neuron* **36**, 649–659 (2002).

14. T. Frank, M. A. Rutherford, N. Strenzke, A. Neef, T. Pangršič, D. Khimich, A. Fejtova, E. D. Gundelfinger, M. C. Liberman, B. Harke, K. E. Bryan, A. Lee, A. Egner, D. Riedel, T. Moser, Bassoon and the synaptic ribbon organize Ca^{2+} channels and vesicles to add release sites and promote refilling. *Neuron* **68**, 724–738 (2010).

15. C. W. Graydon, S. Cho, G.-L. Li, B. Kachar, H. von Gersdorff, Sharp Ca^{2+} nanodomains beneath the ribbon promote highly synchronous multivesicular release at hair cell synapses. *J. Neurosci.* **31**, 16637–16650 (2011).

16. C. Vogl, B. H. Cooper, J. Neef, S. M. Wojcik, K. Reim, E. Reisinger, N. Brose, J.-S. Rhee, T. Moser, C. Wichmann, Unconventional molecular regulation of synaptic vesicle replenishment in cochlear inner hair cells. *J. Cell Sci.* **128**, 638–644 (2015).

17. R. Chakrabarti, L. M. Jaime Tobón, L. Slitin, M. Redondo Canales, G. Hoch, M. Slashcheva, E. Fritsch, K. Bodensiek, Ö. D. Özçete, M. Gültas, S. Michanski, F. Opazo, J. Neef, T. Pangrsic, T. Moser, C. Wichmann, Optogenetics and electron tomography for structure-function analysis of cochlear ribbon synapses. *eLife* **11**, e79494 (2022).

18. J. Neef, N. T. Urban, T.-L. Ohn, T. Frank, P. Jean, S. W. Hell, K. I. Willig, T. Moser, Quantitative optical nanophysiology of Ca^{2+} signaling at inner hair cell active zones. *Nat. Commun.* **9**, 290 (2018).

19. S. Jung, T. Oshima-Takago, R. Chakrabarti, A. B. Wong, Z. Jing, G. Yamanbaeva, M. M. Picher, S. M. Wojcik, F. Göttfert, F. Predoehl, K. Michel, S. W. Hell, S. Schoch, N. Strenzke, C. Wichmann, T. Moser, Rab3-interacting molecules 2α and 2β promote the abundance of voltage-gated $Ca_V1.3$ Ca^{2+} channels at hair cell active zones. *Proc. Natl. Acad. Sci. U.S.A.* **112**, E3141–E3149 (2015).

20. S. Krinner, T. Butola, S. Jung, C. Wichmann, T. Moser, RIM-binding protein 2 promotes a large number of $Ca_V1.3$ Ca^{2+}-channels and contributes to fast synaptic vesicle replenishment at hair cell active zones. *Front. Cell. Neurosci.* **11**, 334 (2017).

21. A. B. Wong, M. A. Rutherford, M. Gabrielaitis, T. Pangršič, F. Göttfert, T. Frank, S. Michanski, S. Hell, F. Wolf, C. Wichmann, T. Moser, Developmental refinement of hair cell synapses tightens the coupling of Ca^{2+} influx to exocytosis. *EMBO J.* **33**, 247–264 (2014).

22. H. Sakamoto, T. Ariyoshi, N. Kimpara, K. Sugao, I. Taiko, K. Takikawa, D. Asanuma, S. Namiki, K. Hirose, Synaptic weight set by Munc13-1 supramolecular assemblies. *Nat. Neurosci.* **21**, 41–49 (2018).

23. A.-H. Tang, H. Chen, T. P. Li, S. R. Metzbower, H. D. MacGillavry, T. A. Blanpied, A trans-synaptic nanocolumn aligns neurotransmitter release to receptors. *Nature* **536**, 210–214 (2016).

24. C. J. Meinrenken, J. G. G. Borst, B. Sakmann, Calcium secretion coupling at calyx of held governed by nonuniform channel-vesicle topography. *J. Neurosci.* **22**, 1648–1667 (2002).

25. L.-Y. Wang, M. J. Fedchyshyn, Y.-M. Yang, Action potential evoked transmitter release in central synapses: Insights from the developing calyx of Held. *Mol. Brain* **2**, 36 (2009).

26. Y. Nakamura, H. Harada, N. Kamasawa, K. Matsui, J. S. Rothman, R. Shigemoto, R. A. Silver, D. A. DiGregorio, T. Takahashi, Nanoscale distribution of presynaptic Ca^{2+} channels and its impact on vesicular release during development. *Neuron* **85**, 145–158 (2015).

27. J. J. Chen, W. A. Kaufmann, C. Chen, I. Arai, O. Kim, R. Shigemoto, P. Jonas, Developmental transformation of Ca^{2+} channel-vesicle nanotopography at a central GABAergic synapse. *Neuron* **112**, 755–771.e9 (2024).

28. T. Miki, W. A. Kaufmann, G. Malagon, L. Gomez, K. Tabuchi, M. Watanabe, R. Shigemoto, A. Marty, Numbers of presynaptic Ca^{2+} channel clusters match those of functionally defined vesicular docking sites in single central synapses. *Proc. Natl. Acad. Sci. U.S.A.* **114**, E5246–E5255 (2017).

29. E. F. Stanley, Single calcium channels and acetylcholine release at a presynaptic nerve terminal. *Neuron* **11**, 1007–1011 (1993).

30. M. L. Harlow, D. Ress, A. Stoschek, R. M. Marshall, U. J. McMahan, The architecture of active zone material at the frog's neuromuscular junction. *Nature* **409**, 479–484 (2001).

31. T. Jarsky, M. Tian, J. H. Singer, Nanodomain control of exocytosis is responsible for the signaling capability of a retinal ribbon synapse. *J. Neurosci.* **30**, 11885–11895 (2010).

32. C. P. Grabner, T. Moser, The mammalian rod synaptic ribbon is essential for Ca_v channel facilitation and ultrafast synaptic vesicle fusion. *eLife* **10**, e63844 (2021).

33. C. P. Grabner, I. Jansen, J. Neef, T. Weihs, R. Schmidt, D. Riedel, C. A. Wurm, T. Moser, Resolving the molecular architecture of the photoreceptor active zone with 3D-MINFLUX. *Sci. Adv.* **8**, eabl7560 (2022).

34. N. Rebola, M. Reva, T. Kirizs, M. Szoboszlay, A. Lőrincz, G. Moneron, Z. Nusser, D. A. DiGregorio, Distinct nanoscale calcium channel and synaptic vesicle topographies contribute to the diversity of synaptic function. *Neuron* **104**, 693–710.e9 (2019).

35. A. Brandt, D. Khimich, T. Moser, Few $Ca_V1.3$ channels regulate the exocytosis of a synaptic vesicle at the hair cell ribbon synapse. *J. Neurosci.* **25**, 11577–11585 (2005).

36. W. M. Roberts, R. A. Jacobs, A. J. Hudspeth, Colocalization of ion channels involved in frequency selectivity and synaptic transmission at presynaptic active zones of hair cells. *J. Neurosci.* **10**, 3664–3684 (1990).

37. T. Pangršič, M. Gabrielaitis, S. Michanski, B. Schwaller, F. Wolf, N. Strenzke, T. Moser, EF-hand protein Ca^{2+} buffers regulate Ca^{2+} influx and exocytosis in sensory hair cells. *Proc. Natl. Acad. Sci. U.S.A.* **112**, E1028–E1037 (2015).

38..Dze te, T. Moser, A sensory cell diversifies its output by varying Ca^{2+} influx-release coupling among active zones. *EMBO J.* **40**, e106010 (2021).

39. L. M. Jaime Tobón, T. Moser, Ca^{2+} regulation of glutamate release from inner hair cells of hearing mice. *Proc. Natl. Acad. Sci. U.S.A.* **120**, e2311539120 (2023).

40. T. Moser, A. Neef, D. Khimich, Mechanisms underlying the temporal precision of sound coding at the inner hair cell ribbon synapse. *J. Physiol.* **576**, 55–62 (2006).

41. D. Beutner, T. Voets, E. Neher, T. Moser, Calcium dependence of exocytosis and endocytosis at the cochlear inner hair cell afferent synapse. *Neuron* **29**, 681–690 (2001).

42. I. Roux, S. Safieddine, R. Nouvian, M. Grati, M.-C. Simmler, A. Bahloul, I. Perfettini, M. Le Gall, P. Rostaing, G. Hamard, A. Triller, P. Avan, T. Moser, C. Petit, Otoferlin, defective in a human deafness form, is essential for exocytosis at the auditory ribbon synapse. *Cell* **127**, 277–289 (2006).

43. N. A. Michalski, J. D. Goutman, S. M. Auclair, J. B. de Monvel, M. Tertrais, A. Emptoz, A. Parrin, S. Nouaille, M. Guillon, M. Sachse, D. Ciric, A. Bahloul, J.-P. Hardelin, R. B. Sutton, P. Avan, S. S. Krishnakumar, J. E. Rothman, D. Dulon, S. Safieddine, C. Petit, Otoferlin acts as a Ca^{2+} sensor for vesicle fusion and vesicle pool replenishment at auditory hair cell ribbon synapses. *eLife* **6**, e31013 (2017).

44. H. Chen, C. Cretu, A. Trebilcock, N. Evdokimova, N. Babai, L. Feldmann, F. Leidner, F. Benseler, S. Mutschall, K. Esch, C. Z. K. Szabo, V. Pena, C. Pape, H. Grubmüller, N. Strenzke, N. Brose, C. Wichmann, J. Preobraschenski, T. Moser, Structure and function of otoferlin, a synaptic protein of sensory hair cells essential for hearing. *Sci. Adv.* **11**, eady8532 (2025).

45. F. Balzarotti, Y. Eilers, K. C. Gwosch, A. H. Gynnå, V. Westphal, F. D. Stefani, J. Elf, S. W. Hell, Nanometer resolution imaging and tracking of fluorescent molecules with minimal photon fluxes. *Science* **355**, 606–612 (2017).

46. K. C. Gwosch, J. K. Pape, F. Balzarotti, P. Hoess, J. Ellenberg, J. Ries, S. W. Hell, MINFLUX nanoscopy delivers 3D multicolor nanometer resolution in cells. *Nat. Methods* **17**, 217–224 (2020).

47. S. Wahl, R. Katiyar, F. Schmitz, A local, periactive zone endocytic machinery at photoreceptor synapses in close vicinity to synaptic ribbons. *J. Neurosci.* **33**, 10278–10300 (2013).

48. N. Holderith, J. Heredi, V. Kis, Z. Nusser, A high-resolution method for quantitative molecular analysis of functionally characterized individual synapses. *Cell Rep.* **32**, 107968 (2020).

49. Y. M. Sigal, C. M. Speer, H. P. Babcock, X. Zhuang, Mapping synaptic input fields of neurons with super-resolution imaging. *Cell* **163**, 493–505 (2015).

50. J. A. Litwin, J. M. Kasprzyk, PAS reaction performed on semithin epon sections following removal of the resin by NaOH in absolute ethanol. *Acta Histochem.* **55**, 98–103 (1975).

51. K. N. Richter, N. H. Revelo, K. J. Seitz, M. S. Helm, D. Sarkar, R. S. Saleeb, E. D’Este, J. Eberle, E. Wagner, C. Vogl, D. F. Lazaro, F. Richter, J. Coy-Vergara, G. Coceano, E. S. Boyden, R. R. Duncan, S. W. Hell, M. A. Lauterbach, S. E. Lehnart, T. Moser, T. F. Outeiro, P. Rehling, B. Schwappach, I. Testa, B. Zapiec, S. O. Rizzoli, Glyoxal as an alternative fixative to formaldehyde in immunostaining and super-resolution microscopy. *EMBO J.* **37**, 139–159 (2018).

52. H. Sobkowicz, J. Rose, G. Scott, S. Slapnick, Ribbon synapses in the developing intact and cultured organ of Corti in the mouse. *J. Neurosci.* **2**, 942–957 (1982).

53. M. A. Rutherford, T. Pangrsic, Molecular anatomy and physiology of exocytosis in sensory hair cells. *Cell Calcium* **52**, 327–337 (2012).

54. S. Michanski, K. Smaluch, A. M. Steyer, R. Chakrabarti, C. Setz, D. Oestreicher, C. Fischer, W. Möbius, T. Moser, C. Vogl, C. Wichmann, Mapping developmental maturation of inner hair cell ribbon synapses in the apical mouse cochlea. *Proc. Natl. Acad. Sci. U.S.A.* **116**, 6415–6424 (2019).

55. M. C. Liberman, Morphological differences among radial afferent fibers in the cat cochlea: An electron-microscopic study of serial sections. *Hear. Res.* **3**, 45–63 (1980).

56. S. Stamataki, H. W. Francis, M. Lehar, B. J. May, D. K. Ryugo, Synaptic alterations at inner hair cells precede spiral ganglion cell loss in aging C57BL/6J mice. *Hear. Res.* **221**, 104–118 (2006).

57. C.-M. Gürth, M. A. do R. B. F. Lima, V. M. Palacios, J. Hubrich, A. R. C. Delgado, N. Mougios, F. Opazo, E. D'Este, Neuronal activity modulates the incorporation of newly translated PSD-95 into a robust structure as revealed by STED and MINFLUX. bioRxiv 562700 [Preprint] (2023). https://doi.org/10.1101/2023.10.18.562700.

58. D. Zenisek, N. K. Horst, C. Merrifield, P. Sterling, G. Matthews, Visualizing synaptic ribbons in the living cell. *J. Neurosci.* **24**, 9752–9759 (2004).

59. H. von Gersdorff, E. Vardi, G. Matthews, P. Sterling, Evidence that vesicles on the synaptic ribbon of retinal bipolar neurons can be rapidly released. *Neuron* **16**, 1221–1227 (1996).

60. C. Limbach, M. M. Laue, X. Wang, B. Hu, N. Thiede, G. Hultqvist, M. W. Kilimann, Molecular in situ topology of Aczonin/Piccolo and associated proteins at the mammalian neurotransmitter release site. *Proc. Natl. Acad. Sci. U.S.A.* **108**, E392–E401 (2011).

61. D. Khimich, R. Nouvian, R. Pujol, S. tom Dieck, A. Egner, E. D. Gundelfinger, T. Moser, Hair cell synaptic ribbons are essential for synchronous auditory signalling. *Nature* **434**, 889–894 (2005).

62. H. Hibino, R. Pironkova, O. Onwumere, M. Vologodskaia, A. J. Hudspeth, F. Lesage, RIM - binding proteins (RBPs) couple Rab3 - interacting molecules (RIMs) to voltage - gated Ca^{2+} channels. *Neuron* **34**, 411–423 (2002).

63. E. Glowatzki, P. A. Fuchs, Transmitter release at the hair cell ribbon synapse. *Nat. Neurosci.* **5**, 147–154 (2002).

64. A. Matsubara, J. H. Laake, S. Davanger, S. Usami, O. P. Ottersen, Organization of AMPA receptor subunits at a glutamate synapse: A quantitative immunogold analysis of hair cell synapses in the rat organ of Corti. *J. Neurosci.* **16**, 4457–4467 (1996).

65. A. C. Meyer, T. Frank, D. Khimich, G. Hoch, D. Riedel, N. M. Chapochnikov, Y. M. Yarin, B. Harke, S. W. Hell, A. Egner, T. Moser, Tuning of synapse number, structure and function in the cochlea. *Nat. Neurosci.* **12**, 444–453 (2009).

66. N. M. Chapochnikov, H. Takago, C.-H. Huang, T. Pangršič, D. Khimich, J. Neef, E. Auge, F. Göttfert, S. W. Hell, C. Wichmann, F. Wolf, T. Moser, Uniquantal release through a dynamic fusion pore is a candidate mechanism of hair cell exocytosis. *Neuron* **17**, 1389–1403 (2014).

67. J. V. Thevathasan, M. Kahnwald, K. Cieśliński, P. Hoess, S. K. Peneti, M. Reitberger, D. Heid, K. C. Kasuba, S. J. Hoerner, Y. Li, Y.-L. Wu, M. Mund, U. Matti, P. M. Pereira, R. Henriques, B. Nijmeijer, M. Kueblbeck, V. J. Sabinina, J. Ellenberg, J. Ries, Nuclear pores as versatile reference standards for quantitative superresolution microscopy. *Nat. Methods* **16**, 1045–1053 (2019).

68. A. H. Clowsley, A. Meletiou, R. Janicek, A. F. E. Bokhobza, E. Lučinskaitė, G. Bleuer, I. Jansen, P. P. Jones, W. E. Louch, C. Soeller, Analysis of RyR2 distribution in HEK293 cells and mouse cardiac myocytes using 3D MINFLUX microscopy. bioRxiv 550636 [Preprint] (2023); https://doi.org/10.1101/2023.07.26.550636.

69. R. Kapoor, T. T. Do, N. Schwenzer, A. Petrovic, T. Dresbach, S. E. Lehnart, R. Fernández-Busnadiego, T. Moser, Establishing synthetic ribbon-type active zones in a heterologous expression system. *eLife* **13**, RP98254 (2025).

70. J. Hellmeier, S. Strauss, S. Xu, L. A. Masullo, E. M. Unterauer, R. Kowalewski, R. Jungmann, Quantification of absolute labeling efficiency at the single-protein level. *Nat. Methods* **21**, 1702–1707 (2024).

71. C. Soeller, A. F. E. Bokhobza, J. Casares-Arias, A. H. Clowsley, Optimizing effective labeling efficiency in MINFLUX 3D DNA-PAINT microscopy by maximizing marker detection probability. bioRxiv 654501 [Preprint] (2025). https://doi.org/10.1101/2025.05.16.654501.

72. J. Tanaka, M. Matsuzaki, E. Tarusawa, A. Momiyama, E. Molnar, H. Kasai, R. Shigemoto, Number and density of AMPA receptors in single synapses in immature cerebellum. *J. Neurosci.* **25**, 799–807 (2005).

73. R. P. Seal, O. Akil, E. Yi, C. M. Weber, L. Grant, J. Yoo, A. Clause, K. Kandler, J. L. Noebels, E. Glowatzki, L. R. Lustig, R. H. Edwards, Sensorineural deafness and seizures in mice lacking vesicular glutamate transporter 3. *Neuron* **57**, 263–275 (2008).

74. J. Ruel, S. Emery, R. Nouvian, T. Bersot, B. Amilhon, J. M. Van Rybroek, G. Rebillard, M. Lenoir, M. Eybalin, B. Delprat, T. A. Sivakumaran, B. Giros, S. El Mestikawy, T. Moser, R. J. H. Smith, M. M. Lesperance, J.-L. Puel, Impairment of SLC17A8 encoding vesicular glutamate transporter-3, VGLUT3, underlies nonsyndromic deafness DFNA25 and inner hair cell dysfunction in null mice. *Am. J. Hum. Genet.* **83**, 278–292 (2008).

75. N. Obholzer, S. Wolfson, J. G. Trapani, W. Mo, A. Nechiporuk, E. Busch-Nentwich, C. Seiler, S. Sidi, C. Söllner, R. N. Duncan, A. Boehland, T. Nicolson, Vesicular glutamate transporter 3 is required for synaptic transmission in zebrafish hair cells. *J. Neurosci.* **28**, 2110–2118 (2008).

76. T. Pangrsic, L. Lasarow, K. Reuter, H. Takago, M. Schwander, D. Riedel, T. Frank, L. M. Tarantino, J. S. Bailey, N. Strenzke, N. Brose, U. Müller, E. Reisinger, T. Moser, Hearing

requires otoferlin-dependent efficient replenishment of synaptic vesicles in hair cells. *Nat. Neurosci.* **13**, 869–876 (2010).

77. N. H. Revelo, D. Kamin, S. Truckenbrodt, A. B. Wong, K. Reuter-Jessen, E. Reisinger, T. Moser, S. O. Rizzoli, A new probe for super-resolution imaging of membranes elucidates trafficking pathways. *J. Cell Biol.* **205**, 591–606 (2014).

78. S. Takamori, M. Holt, K. Stenius, E. A. Lemke, M. Grønborg, D. Riedel, H. Urlaub, S. Schenck, B. Brügger, P. Ringler, Molecular anatomy of a trafficking organelle. *Cell* **127**, 831–846 (2006).

79. A. Baddeley, P. J. Diggle, A. Hardegen, T. Lawrence, R. K. Milne, G. Nair, On tests of spatial pattern based on simulation envelopes. *Ecological monographs* **84**, 477–489 (2014).

80. R. A. Kerr, T. M. Bartol, B. Kaminsky, M. Dittrich, J.-C. J. Chang, S. B. Baden, T. J. Sejnowski, J. R. Stiles, Fast Monte Carlo simulation methods for biological reaction-diffusion systems in solution and on surfaces. *SIAM J. Sci. Comput.* **30**, 3126–3149 (2008).

81. T. Moser, D. Beutner, Kinetics of exocytosis and endocytosis at the cochlear inner hair cell afferent synapse of the mouse. *Proc. Natl. Acad. Sci. U.S.A.* **97**, 883–888 (2000).

82. L. M. Jaime Tobón, T. Moser, Bridging the gap between presynaptic hair cell function and neural sound encoding. *eLife* **12**, RP93749 (2024).

83. J. E. Heuser, T. S. Reese, M. J. Dennis, Y. Jan, L. Jan, L. Evans, Synaptic vesicle exocytosis captured by quick freezing and correlated with quantal transmitter release. *J. Cell Biol.* **81**, 275–300 (1979).

84. R. Nouvian, J. Neef, A. V. Bulankina, E. Reisinger, T. Pangršič, T. Frank, S. Sikorra, N. Brose, T. Binz, T. Moser, Exocytosis at the hair cell ribbon synapse apparently operates without neuronal SNARE proteins. *Nat. Neurosci.* **14**, 411–413 (2011).

85. C. Calvet, T. Peineau, N. Benamer, M. Cornille, A. Lelli, B. Plion, G. Lahlou, J. Fanchette, S. Nouaille, J. B. de Monvel, A. Estivalet, P. Jean, V. Michel, M. Sachse, N. Michalski, P. Avan,

C. Petit, D. Dulon, S. Safieddine, The SNARE protein SNAP-25 is required for normal exocytosis at auditory hair cell ribbon synapses. *iScience* **25**, 105628 (2022).

86. E. Reisinger, C. Bresee, J. Neef, R. Nair, K. Reuter, A. Bulankina, R. Nouvian, M. Koch, J. Bückers, L. Kastrup, I. Roux, C. Petit, S. W. Hell, N. Brose, J.-S. Rhee, S. Kügler, J. V. Brigande, T. Moser, Probing the functional equivalence of otoferlin and synaptotagmin 1 in exocytosis. *J. Neurosci.* **31**, 4886–4895 (2011).

87. M. Beurg, N. Michalski, S. Safieddine, Y. Bouleau, R. Schneggenburger, E. R. Chapman, C. Petit, D. Dulon, Control of exocytosis by synaptotagmins and otoferlin in auditory hair cells. *J. Neurosci.* **30**, 13281–13290 (2010).

88. N. Strenzke, S. Chanda, C. Kopp-Scheinpflug, D. Khimich, K. Reim, A. V. Bulankina, A. Neef, F. Wolf, N. Brose, M. A. Xu-Friedman, T. Moser, Complexin-I is required for high-fidelity transmission at the Endbulb of held auditory synapse. *J. Neurosci.* **29**, 7991–8004 (2009).

89. A. P. Cepeda, M. Ninov, J. Neef, I. Parfentev, K. Kusch, E. Reisinger, R. Jahn, T. Moser, H. Urlaub, Proteomic analysis reveals the composition of glutamatergic organelles of auditory inner hair cells. *Mol. Cell. Proteomics* **23**, 100704 (2024).

90. S. Safieddine, R. J. Wenthold, SNARE complex at the ribbon synapses of cochlear hair cells: Analysis of synaptic vesicle- and synaptic membrane-associated proteins. *Eur. J. Neurosci.* **11**, 803–812 (1999).

91. R. C. Uthaiah, A. J. Hudspeth, Molecular anatomy of the hair cell's ribbon synapse. *J. Neurosci.* **30**, 12387–12399 (2010).

92. T. Moser, "Presynaptic physiology of cochlear inner hair cells," in *The Senses: A Comprehensive Reference* (Elsevier, 2020), pp. 441–467. https://linkinghub.elsevier.com/retrieve/pii/B9780128093245241850.

93. J.-C. Leclère, D. Dulon, Otoferlin as a multirole Ca^{2+} signaling protein: From inner ear synapses to cancer pathways. *Front. Cell. Neurosci.* **17**, 1197611 (2023).

94. S. Yasunaga, M. Grati, M. Cohen-Salmon, A. El-Amraoui, M. Mustapha, N. Salem, E. El-Zir, J. Loiselet, C. Petit, A mutation in OTOF, encoding otoferlin, a FER-1-like protein, causes DFNB9, a nonsyndromic form of deafness. *Nat. Genet.* **21**, 363–369 (1999).

95. B. G. Wilhelm, S. Mandad, S. Truckenbrodt, K. Kröhnert, C. Schäfer, B. Rammner, S. J. Koo, G. A. Claßen, M. Krauss, V. Haucke, H. Urlaub, S. O. Rizzoli, Composition of isolated synaptic boutons reveals the amounts of vesicle trafficking proteins. *Science* **344**, 1023–1028 (2014).

96. T. Frank, D. Khimich, A. Neef, T. Moser, Mechanisms contributing to synaptic Ca^{2+} signals and their heterogeneity in hair cells. *Proc. Natl. Acad. Sci. U.S.A.* **106**, 4483–4488 (2009).

97. T.-L. Ohn, M. A. Rutherford, Z. Jing, S. Jung, C. J. Duque-Afonso, G. Hoch, M. M. Picher, A. Scharinger, N. Strenzke, T. Moser, Hair cells use active zones with different voltage dependence of Ca^{2+} influx to decompose sounds into complementary neural codes. *Proc. Natl. Acad. Sci. U.S.A.* **113**, E4716–E4725 (2016).

98. T. Moser, N. Karagulyan, J. Neef, L. M. Jaime Tobón, Diversity matters — Extending sound intensity coding by inner hair cells via heterogeneous synapses. *EMBO J.* **42**, e114587 (2023).

99. N. Karagulyan, A. Thirumalai, S. Michanski, Y. Qi, Q. Fang, H. Wang, N. J. Ortner, J. Striessnig, N. Strenzke, C. Wichmann, Y. Hua, T. Moser, Gating of hair cell Ca^{2+} channels governs the activity of cochlear neurons. *Sci. Adv.* **11**, eadu7898 (2025).

100. M. Lelek, M. T. Gyparaki, G. Beliu, F. Schueder, J. Griffié, S. Manley, R. Jungmann, M. Sauer, M. Lakadamyali, C. Zimmer, Single-molecule localization microscopy. *Nat. Rev. Methods Primers* **1**, 39 (2021).

101. J. Wang, H. Zou, X. Fu, C. Gu, L. Yao, S. Li, Q. Zhang, M. Gu, MINFLUX reveals nonnormal distribution of linkage errors in immunofluorescence labeling. *Commun. Phys.* **8**, 253 (2025).

102. G. V. Los, L. P. Encell, M. G. McDougall, D. D. Hartzell, N. Karassina, C. Zimprich, M. G. Wood, R. Learish, R. F. Ohana, M. Urh, D. Simpson, J. Mendez, K. Zimmerman, P. Otto, G. Vidugiris, J. Zhu, A. Darzins, D. H. Klaubert, R. F. Bulleit, K. V. Wood, HaloTag: A novel protein labeling technology for cell imaging and protein analysis. *ACS Chem. Biol.* **3**, 373–382 (2008).

103. S. Krinner, F. Predoehl, D. Burfeind, C. Vogl, T. Moser, RIM-binding proteins are required for normal sound-encoding at afferent inner hair cell synapses. *Front. Mol. Neurosci.* **14**, 651935 (2021).

104. D. Davydova, C. Marini, C. King, J. Klueva, F. Bischof, S. Romorini, C. Montenegro-Venegas, M. Heine, R. Schneider, M. S. Schröder, W. D. Altrock, C. Henneberger, D. A. Rusakov, E. D. Gundelfinger, A. Fejtova, Bassoon specifically controls presynaptic P/Q-type Ca^{2+} channels via RIM-binding protein. *Neuron* **82**, 181–194 (2014).

105. X. Wu, Q. Cai, Z. Shen, X. Chen, M. Zeng, S. Du, M. Zhang, RIM and RIM-BP form presynaptic active-zone-like condensates via phase separation. *Mol. Cell* **73**, 971–984.e5 (2019).

106. T. Ghelani, M. Escher, U. Thomas, K. Esch, J. Lützkendorf, H. Depner, M. Maglione, P. Parutto, S. Gratz, T. Matkovic-Rachid, S. Ryglewski, A. M. Walter, D. Holcman, K. O'Connor Giles, M. Heine, S. J. Sigrist, Interactive nanocluster compaction of the ELKS scaffold and cacophony Ca^{2+} channels drives sustained active zone potentiation. *Sci. Adv.* **9**, eade7804 (2023).

107. J. Heck, P. Parutto, A. Ciuraszkiewicz, A. Bikbaev, R. Freund, J. Mitlöhner, M. Andres-Alonso, A. Fejtova, D. Holcman, M. Heine, Transient confinement of $Ca_V2.1$ Ca^{2+}-channel splice variants shapes synaptic short-term plasticity. *Neuron* **103**, 66–79.e12 (2019).

108. N. Schwenzer, R. Tsukanov, T. Kohl, S. Basak, F. Seibertz, N. Voigt, J. Enderlein, S. E. Lehnart, Nanoscale architecture and dynamics of CaV1.3 channel clusters in cardiac myocytes revealed by single channel nanoscopy. bioRxiv 582084 [Preprint] (2024). https://doi.org/10.1101/2024.02.26.582084.

109. S. Jung, T. Maritzen, C. Wichmann, Z. Jing, A. Neef, N. H. Revelo, H. Al-Moyed, S. Meese, S. M. Wojcik, I. Panou, H. Bulut, P. Schu, R. Ficner, E. Reisinger, S. O. Rizzoli, J. Neef, N. Strenzke, V. Haucke, T. Moser, Disruption of adaptor protein 2μ (AP-2μ) in cochlear hair cells impairs vesicle reloading of synaptic release sites and hearing. *EMBO J.* **34**, 2686–2702 (2015).

110. L. M. Ostersehlt, D. C. Jans, A. Wittek, J. Keller-Findeisen, K. Inamdar, S. J. Sahl, S. W. Hell, S. Jakobs, DNA-PAINT MINFLUX nanoscopy. *Nat. Methods* **19**, 1072–1075 (2022).

111. C. S. Mesnard, C. L. Barta, A. L. Sladek, D. Zenisek, W. B. Thoreson, Eliminating synaptic ribbons from rods and cones halves the releasable vesicle pool and slows down replenishment. *Int. J. Mol. Sci.* **23**, 6429 (2022).

112. C. Fasano, J. Rocchetti, K. Pietrajtis, J.-F. Zander, F. Manseau, D. Y. Sakae, M. Marcus-Sells, L. Ramet, L. J. Morel, D. Carrel, S. Dumas, S. Bolte, V. Bernard, E. Vigneault, R. Goutagny, G. Ahnert-Hilger, B. Giros, S. Daumas, S. Williams, S. El Mestikawy, Regulation of the hippocampal network by VGLUT3-positive CCK- GABAergic basket cells. *Front. Cell. Neurosci.* **11**, 140 (2017).

113. R. Schmidt, T. Weihs, C. A. Wurm, I. Jansen, J. Rehman, S. J. Sahl, S. W. Hell, MINFLUX nanometer-scale 3D imaging and microsecond-range tracking on a common fluorescence microscope. *Nat. Commun.* **12**, 1478 (2021).

114. A. Ponti, J. C. Arias, T. Horn, pyMINFLUX, version the latest one. https://doi.org/10.5281/zenodo.7895501.

115. J. Ahrens, B. Geveci, C. Law, “ParaView: An end-user tool for large data visualization,” in *The Visualization Handbook,* (Academic Press/Elsevier, 2005), pp. 717–731.

116. M. Ester, H.-P. Kriegel, J. Sander, X. Xu, “A density-based algorithm for discovering clusters in large spatial databases with noise,” in *KDD’96: Proceedings of the Second International Conference on Knowledge Discovery and Data Mining* (AAAI Press, 1996), pp. 226–231.

117. F. Pedregosa, V. Gaël, A. Gramfort, V. Michel, B. Thirion, O. Grisel, M. Blondel, P. Prettenhofer, R. Weiss, V. Dubourg, J. Vanderplas, A. Passos, D. Cournapeau, M. Brucher, M. Perrot, É. Duchesnay, Scikit-learn: Machine learning in Python. *J. Mach. Learn. Res.* **12**, 2825–2830 (2011).

118. V. Zampini, S. L. Johnson, C. Franz, N. D. Lawrence, S. Münkner, J. Engel, M. Knipper, J. Magistretti, S. Masetto, W. Marcotti, Elementary properties of Ca_V1.3 Ca^{2+} channels expressed in mouse cochlear inner hair cells. *J. Physiol.* **588**, 187–199 (2010).

119. D. J. Jagger, D. Robertson, G. D. Housley, A technique for slicing the rat cochlea around the onset of hearing. *J. Neurosci. Methods* **104**, 77–86 (2000).

120. A. Scimemi, J. S. Diamond, The number and organization of Ca^{2+} channels in the active zone shapes neurotransmitter release from Schaffer collateral synapses. *J. Neurosci.* **32**, 18157–18176 (2012).

121. S. Vidal, M. Lombardero, P. Sánchez, A. Román, L. Moya, An easy method for the removal of Epon resin from semi-thin sections. Application of the avidin-biotin technique. *Histochem. J.* **27**, 204–209 (1995).

122. E. A. Lumpkin, A. J. Hudspeth, Regulation of free Ca^{2+} concentration in hair-cell stereocilia. *J. Neurosci.* **18**, 6300–6318 (1998).

123. D. Novo, M. DiFranco, J. L. Vergara, Comparison between the predictions of diffusion-reaction models and localized Ca^{2+} transients in amphibian skeletal muscle fibers. *Biophys. J.* **85**, 1080–1097 (2003).

124. U. V. Nägerl, D. Novo, I. Mody, J. L. Vergara, Binding kinetics of calbindin-D28k determined by flash photolysis of caged Ca^{2+}. *Biophys. J.* **79**, 3009–3018 (2000).

125. M. Naraghi, T-jump study of calcium binding kinetics of calcium chelators. *Cell Calcium* **22**, 255–268 (1997).

126. S. M. Baylor, S. Hollingworth, Model of sarcomeric Ca^{2+} movements, including ATP Ca^{2+} binding and diffusion, during activation of frog skeletal muscle. *J. Gen. Physiol.* **112**, 297–316 (1998).

127. N. L. Allbritton, T. Meyer, L. Stryer, Range of messenger action of calcium ion and inositol 1,4,5-trisphosphate. *Science* **258**, 1812–1815 (1992).